Chemically Driven Interfacial Coupling in Charge-Transfer Mediated Functional Superstructures

Beibei Xu,[†] Huashan Li,[‡] Haoqi Li,[†] Andrew J. Wilson,[§] Lin Zhang,[†] Ke Chen,[||] Katherine A. Willets,[§] Fei Ren,[†] Jeffrey C. Grossman,*[,‡] and Shenqiang Ren*[,†]

[†]Department of Mechanical Engineering and Temple Materials Institute, Temple University, Philadelphia, Pennsylvania 19122, United States

[‡]Department of Materials Science and Engineering, Massachusetts Institute of Technology, Cambridge, Massachusetts 02139 United States

[§]Department of Chemistry, Temple University, Philadelphia, Pennsylvania 19122, United States

[||]Department of Physics and Temple Materials Institute, Temple University, Philadelphia, Pennsylvania 19122, United States

S Supporting Information

ABSTRACT: Organic charge-transfer superstructures are enabling new interfacial electronics, such as organic thermoelectrics, spin-charge converters, and solar cells. These carbon-based materials could also play an important role in spin-based electronics due to their exceptionally long spin lifetime. However, to explore these potentials a coherent design strategy to control interfacial charge-transfer interaction is indispensable. Here we report that the control of organic crystallization and interfacial electron coupling are keys to dictate external stimuli responsive behaviors in organic charge-transfer superstructures. The integrated experimental and computational study reveals the importance of chemically driven interfacial coupling in organic charge-transfer superstructures. Such degree of engineering opens up a new route to develop a new generation of functional charge-transfer materials, enabling important advance in all organic interfacial electronics.

**KEYWORDS:** *Nanoferroics, organic crystallization, materials design, and multifuctionality*
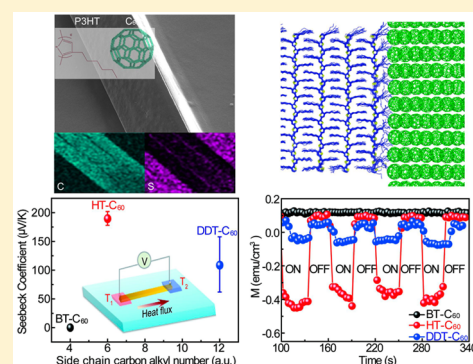
The mixing of conductivity and ferroic orders in functional materials could lead to numerous technological advances, such as ferroic field-effect transistors and magnetoelectric tunnel junctions.[1−4] However, the ferroic orders are related to the interaction of localized electrons while the conduction is determined by the movement of electrons; thus, simultaneous conducting and ferroic orders remains challenging in conventional materials. Materials-by-design and assembly principle provides a unique and exciting opportunity, as it allows us to design novel multifunctional organic materials that combine two or more physical properties in the same crystal lattice, which are difficult or impossible to achieve in continuous inorganic crystalline solids. Organic charge transfer (CT) assemblies, consisting of an electron donor and acceptor with π-electron orbitals, can possess both charge and spin orders due to the largely delocalized π-electrons and the exchange interaction.[5,6] Over the past decades, numerous materials have been designed toward the development of functional CT complexes.[7,8] Recently, room-temperature multiferroicity in centimeter-sized crystalline charge-transfer superstructures, consisting of polymer−fullerene complexes, was achieved by the self-organization and molecular-packing induced charge order-driven ferroic coupling.[9] To take advantage of the complexity and tunability of this new class of organic functional materials, a comprehensive understanding of the relationship between structure and properties is important.

Interfacial engineering has been widely used to tune the electronic and optical behaviors of polymer−fullerene-based CT devices, and materials-by-design criteria exhibit a strong dependence on their structural architecture as demonstrated by both experimental[10−14] and theoretical[15−19] studies. Typically, longer side chain lengths of polymers lead to higher fullerene mobility and thus a larger scale of phase separation that reduces the interfacial area for charge separation.[20] Despite the novel properties observed in polymer−fullerene-based CT structures, a systematic analysis regarding the design strategy of polymer side-chain engineering is lacking. The conclusions obtained by previous studies on blend films cannot necessarily be applied to the CT superstructures because (1) although diffusion of C_{60} molecules is important to determine the morphology of traditional blends, it is a negligible effect in the CT superstructures as the C_{60}s are packed inside the crystal domains; (2) unlike the relatively fixed donor−acceptor distance in traditional blends with the π-stacking direction perpendicular to the interface,[17] the lengths of side-chains
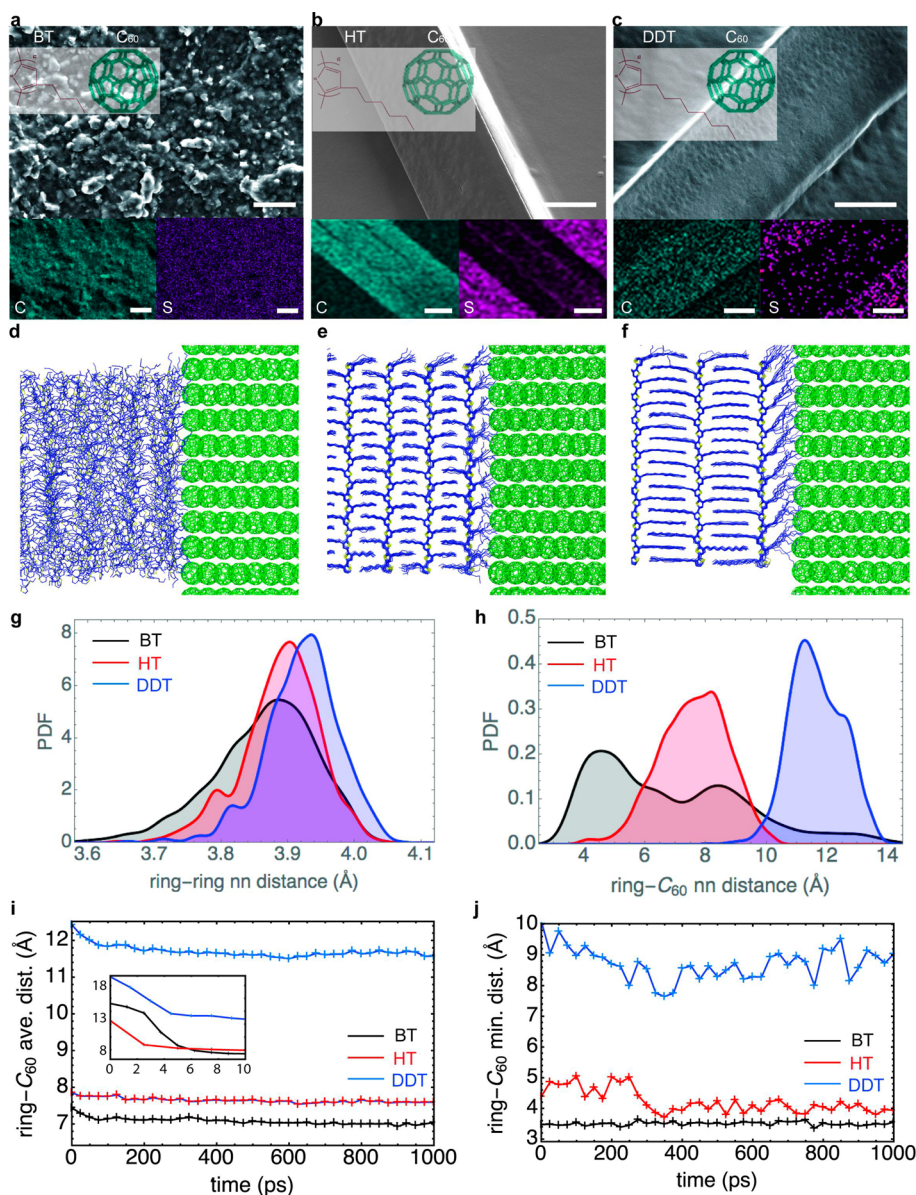
Figure 1. Crystal structure, morphology, chemical analysis of charge transfer complexes, and microscopic structural information on CT superstructures. (a–c) SEM and EDS element map of BT-C_{60}, HT-C_{60}, and DDT-C_{60} complexes, respectively. The insets are the structural formula of BT, HT, DDT and fullerene (C_{60}). The scale bars in panels a–c are 10, 50, and 30 μm, respectively. (d–f) Snapshot of disordered BT-C_{60}, crystallized HT-C_{60}, and crystallized DDT-C_{60} interfaces at t = 1 ns, respectively. C_{60}, green; C in P3XT, blue; S in P3XT, yellow. (g,h) Probability density function of distance between nn rings in polymer phases and between rings and nn C_{60} molecule at BT-C_{60}, HT-C_{60}, and DDT-C_{60} interfaces, respectively. (i,j) Evolution of averaged ring-C_{60} distance after early time stage of NPT simulations with those during early time stage shown in the inset, and minimum ring-C_{60} distance after early time stage, respectively.

determine the donor−acceptor distances in the CT super-structures as the π-stacking direction is nearly parallel to the interface, and thus may substantially affect the electron coupling for charge transfer and intersystem crossing. In this work, we shed light on the impact of chemically driven side-chain engineering on correlated optical, thermal, electric and magnetic properties of CT superstructures using a combined experimental and theoretical approach. The CT superstructures with crystallization between fullerene (C_{60}) acceptor and polythiophene donor with varying alkyl side chains were chosen as prototype systems since exceptional optoelectronic response and optical characteristics have been observed in these π-conjugated systems.[21,22] Our results suggest that the essential strategy for side-chain design to dictate external stimuli

responsive behavior is control over polymer crystallization and interfacial electron coupling. Moreover, the Seebeck coefficients observed in such CT superstructures are among the highest reported for polymeric thermoelectric materials.

In order to probe the effect of alkyl side-chain length on donor−donor and donor−acceptor couplings, we examine the following electron donors: poly(3-butylthiophene-2,5-diyl) (BT), poly(3-hexylthiophene-2,5-diyl) (HT), and poly(3-dodecylthiophene-2,5-diyl) (DDT) with side chains consisting of 4, 6, and 12 carbon alkyls, respectively (shown in the inset of Figure 1a−c). The antisolvent crystallization combined with the solvent vapor evaporation approach is employed to obtain the CT superstructures. In comparison to the randomly distributed particle-like formation of BT-C_{60} complex (Figure 1a and
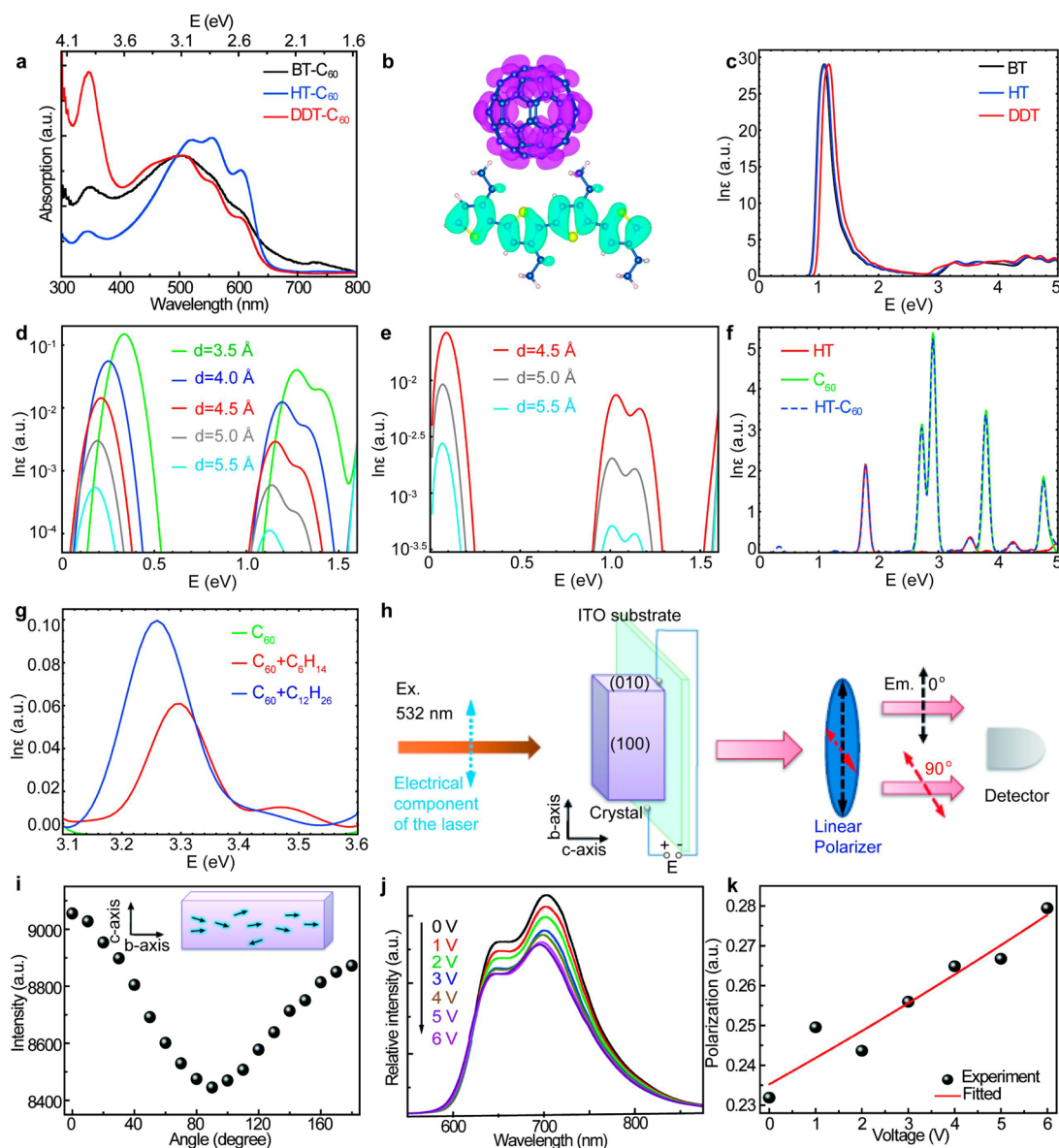
Figure 2. Optical properties of charge transfer complexes. (a) Absorption spectra of BT-C_{60}, HT-C_{60}, and DDT-C_{60} complexes. (b) HOMO (in cyan) and LUMO (in magenta) wave functions of the pair of truncated polymer and C_{60} molecule with the side-chains perpendicular to the interface. (c) Calculated absorption spectra of BT, HT, and DDT crystals. (d,e) Calculated donor−acceptor distance-dependent absorption spectra of pairs of truncated polymers and C_{60} molecules associated with charge transfer states with the side-chains parallel (d) and perpendicular (e) to the interface. (f) Comparison of calculated absorption spectra between the combined system shown in (b) and its isolated components. (g) Calculated absorption spectra relevant to charge transfer states at the interfaces between a C_{60} molecule and an alkyl chain containing 6/12 C atoms. (h) Scheme for the fluorescence measurements with an applied voltage. The electric component of the excitation laser is parallel to the crystal growth direction. The emission light is detected through a polarizer set to an angle of 0° or 90° with respect to the electric component of the excitation laser. Electrical leads are attached such that the voltage is applied along the b-axis of the crystal. The actual fluorescence experiment is performed in a backscattering configuration but is drawn as forward scattering for clarity. (i) Excitation polarization (0°−180°) dependent fluorescence intensity of the HT-C_{60} crystal. The values of 0° and 90° correspond to the b-axis and a-axis of HT-C_{60} crystal, respectively. The small arrows in the crystal denote dipoles. (j) Electric field-dependent photoluminescence for the 0° emission of the HT-C_{60} crystal. (k) The polarization ratio change for the emission intensity at 700 nm. The ratio increases with an increase of applied voltage. The voltage is applied parallel to the crystal growth direction.

Figure S2), the HT-C_{60} and DDT-C_{60} complexes enable well-defined needle-like crystal formation (Figure 1b,c, and Figure S3−S4). Figure 1a−c shows scanning electron microscopy (SEM) images and the carbon and sulfur chemical analysis mapping from energy dispersive X-ray spectroscopy (EDS) of BT-C_{60}, HT-C_{60}, and DDT-C_{60}, respectively, in which the phase identification is confirmed by X-ray diffraction (XRD, Figure S1). On the basis of the insights from these crystal structure measurements, we further probe the origin of

microscopic crystalline formation of these superstructure phases using classical molecular dynamics (MD) (the detailed simulation methods are described in the Supporting Information Section 5.1). Because of the strong attraction between molecules inside each phase and the steric repulsion between polymer side-chains and C_{60} molecules, phase separations are stable regardless of the degree of crystallization of the polymers during the 1 ns simulations within the isothermal−isobaric (NPT) ensemble, as shown in Figure 1d for disordered BT and
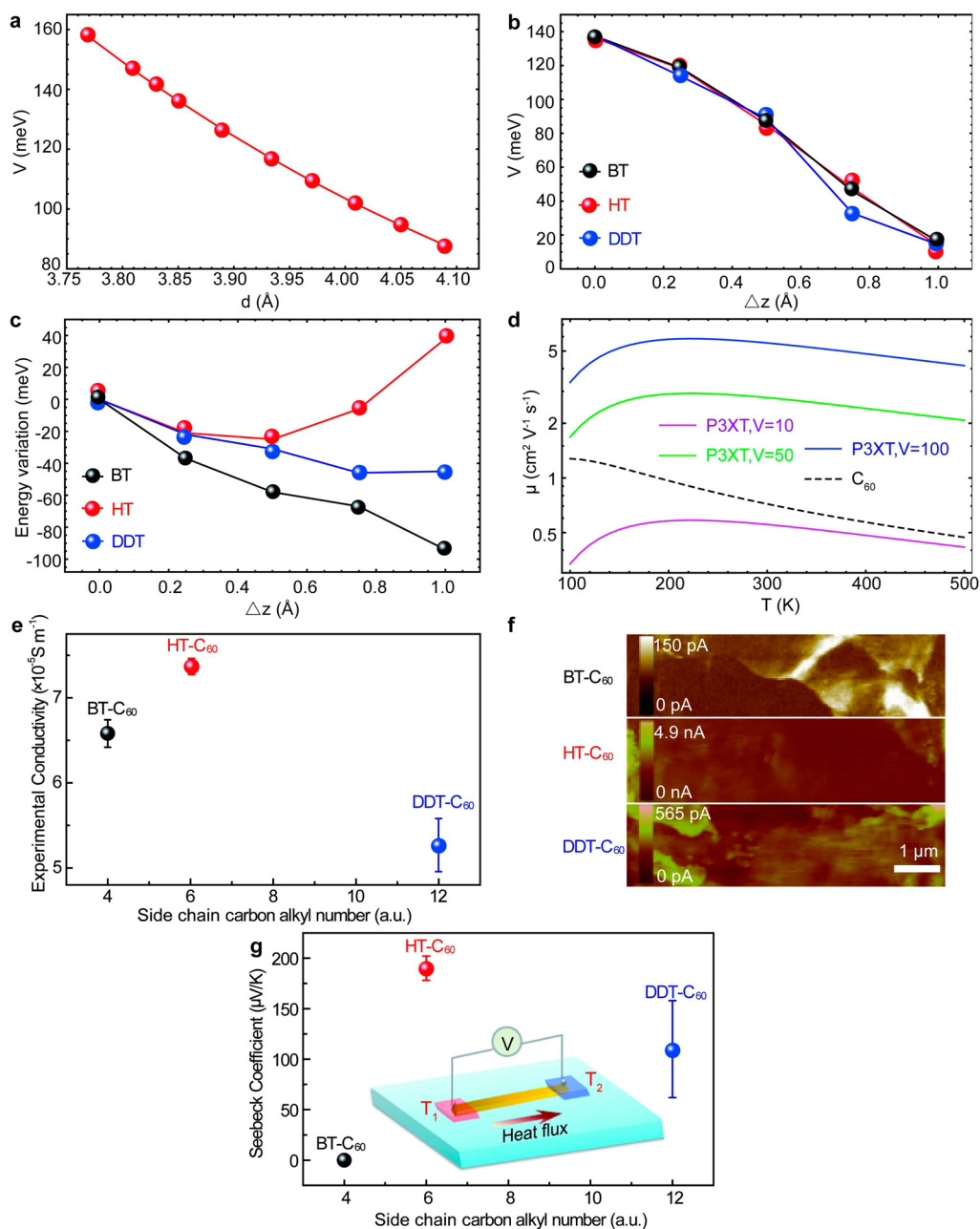
Figure 3. Electron transport properties. (a) Calculated electron coupling between truncated P3HT with different π-stacking distance. (b) Calculated Δz (shift between neighboring polymers along the backbone direction) dependent electron coupling between truncated polythiophene molecules containing eight rings. (c) Computed total energy variation of polythiophene crystals versus Δz referred to zero-shift configuration. (d) Calculated electron coupling (in units of meV) dependent hole mobility for the polythiophene crystal phases and electron mobility for the C_{60} phase. (e) Experimental conductivity of BT-C_{60}, HT-C_{60}, and DDT-C_{60} complexes with alkyl side chain containing 4, 6, and 12 carbon alkyls. (f) AFM and conducting AFM of BT-C_{60}, HT-C_{60}, and DDT-C_{60} complexes, respectively. (g) Effect of side chain length on the room temperature Seebeck coefficient of BT-C_{60}, HT-C_{60}, and DDT-C_{60} complexes, respectively. The inset is the measurement scheme of thermoelectric effect.

Figures 1e,f for ordered HT/DDT, respectively. The distances between nearest neighboring (nn) five-member rings are slightly larger in DDT than in HT, whereas a much broader profile is observed in disordered BT (Figure 1g). Starting from a spacing of about 0.3 nm, the polymer−C_{60} interfacial structures relax quickly within 10 ps and evolve very slowly afterward (Figure 1i). The distances between rings and their nn C_{60} molecules at the DDT-C_{60} interface are much larger than those at the HT-C_{60} interface but follow a similar Gaussian distribution.[9] By contrast, the ring-C_{60} distance distribution at the disordered BT-C_{60} interface is much broader and irregular,

with a larger proportion in small distances that tends to increase with increasing time (Figure 1h and Figure S12). While the head-to-head defects at the polymer−C_{60} interface also increase the probability of short ring-C_{60} distances, the effect is much less significant than the disordered initial condition (Figure S14). These results provide a qualitative scenario of how the modification of side-chain chemistry affects the microscopic structure in two aspects, the crystallization of the polymer and the donor−acceptor distance. Next we focus on how such subtle changes in microscopic structure result in a wide range of physical properties.

Although the alkyl side chains are electronically inert, the measured absorption spectra for BT-C_{60}, HT-C_{60}, and DDT-C_{60} complexes are remarkably different from one another as shown in Figure 2a. To understand this phenomenon, we compute the absorption spectra of crystallized polymers with infinite lengths, and pairs of truncated polymer and C_{60} molecules, by ab initio simulations using the random phase approximation (RPA). Although RPA does not accurately predict the optical gaps, it gives a similar strength of CT absorption to those obtained by the more accurate GW-BSE method in previous studies on HT-C_{60} interfaces[23] and thus serves as a sufficient method for our purpose of qualitatively identifying the origin of absorption peaks. Because the calculated spectra for crystallized polymers exhibit only slight variations of near-edge absorption caused by different stacking distances, the strongest absorption at 450−600 nm observed in HT-C_{60} is likely due to the highest packing density, while the broadening of the absorption peak can be ascribed to the wide range of conjugation lengths in the disordered system. Notice that only BT-C_{60} provides absorption peaks in the infrared range, which may originate from the direct generation of CT states as illustrated in Figure 2d−f. Such excitation requires sufficient electron coupling between the highest occupied molecular orbital (HOMO) localized on the polymer and the lowest unoccupied molecular orbital (LUMO) localized on C_{60} (Figure 2b), which decays sharply with increasing donor−acceptor distance (Figure 2d,e, Supporting Information Section 5.3) and thus can only occur in disordered BT-C_{60} super-structures with unique donor−acceptor separation profiles. The broad absorption spectrum of the BT-C_{60} complex reveals enhanced charge transfer interaction (Figure 2a), resulting from the short side chain enhanced π-electron density and decreased shielding effects from donating electrons to acceptors.[24] In addition, the strong UV absorption in the DDT-C_{60} super-structures can be understood from the alkyl chain related transitions either within the polymer (Figure 2c) or at the donor−acceptor interface (Figure 2g). The effect of the alkyl side chain on molecular packing can influence the optical anisotropy of CT crystalline superstructures. The 532 nm excitation light polarization is rotated in 10° increments with respect to the crystal growth axis (defined as 0°) and the resulting emission intensity is measured (Figure 2h). Figure 2i shows the representative data for a HT-C_{60} crystal in which the fluorescence intensity reaches a maximum (minimum) when the excitation polarization is parallel (perpendicular) to the crystal growth axis, indicating a slight preferential alignment of the transition dipoles along the direction of the crystal growth. The emission is also slightly polarized in this sample, as determined by aligning the excitation polarization along the b-axis of the crystal (e.g., 0°) and collecting the fluorescence emission polarized either parallel or perpendicular to the excitation (Figure S6a). These results are consistent with the previous report that the polythiophene−C_{60} CT super-structures are self-organized through the $\pi-\pi$ conjugated interaction along the b-axis (crystal growth direction) and stacked in planar structures with the long chain axis (c-axis) nearly perpendicular to the substrate.[9] While the fluorescence emission is also polarized for the DDT-C_{60} crystal, the BT-C_{60} crystal shows no preferential emission polarization, consistent with the disordered nature of this material (Figure S6e,f). Furthermore, the change in fluorescence from a single HT-C_{60} crystal measured as an external electric potential is applied. The excitation polarization is fixed parallel to the crystal's b-axis and

the fluorescence is collected through a linear polarizer set either parallel (0°) or perpendicular (90°) with respect to the excitation (Figure 2h). Figure 2j,k shows the external electric potential-dependent emission of a HT-C_{60} crystal. As the electric field increases, the emission intensity at both 0° and 90° decreases (Figure 2j and Figure S7, respectively), which we attribute to the increased dissociation of excitons at the CT interface. The polarization ratio (P) is then calculated from the intensity of the emission at 700 nm, polarized either parallel (I_0) or perpendicular (I_{90}) as follows

$$P = \frac{(I_0 - I_{90})}{(I_0 + I_{90})} \tag{1}$$

The polarization ratio increases linearly with applied voltage, indicating that anisotropic emission can be induced in these materials through application of an applied field (Figure 2k).

The side-chains of polythiophene are also known to play a critical role in the carrier transport.[10,12,14] Though both density functional theory (DFT) and molecular dynamics (MD) simulations have been implemented to probe the electronic structure and packing order of HT crystals,[18,19,25] the atomistic-scale understanding of how the side-chains affect the carrier mobility has received less attention. To address this potential, we apply the phonon-assisted charge transfer model with a full quantum treatment,[26,27] wherein the hopping rate is dictated by the electron coupling and reorganization energy (Supporting Information Section 5.4). The most straightforward side-chain effect is increasing π-stacking distance with increasing side chain length,[28] which results in a weak electron coupling (Figure 3a). Though the shift between neighboring polymer along the backbone direction (Figure 3b) is weak, it can still substantially reduce the electron coupling caused by insufficient wave function overlap (Figure 3c). Interestingly, the energy profile versus shift distance exhibits a nonmonotonic trend with side-chain length (Figure 3c), which can be explained by the fact that the deviation from ideal crystal structure reduces the steric repulsion between nn ligands but increases the steric energy between dentate units. In addition to the local effects, side-chains also change the crystallinity of the polymer and thus the conjugation length. As summarized in Table 1, electron

Table 1. Electronic Coupling (V) between Two Truncated Polymers and Reorganization Energy (λ) of Hole Hopping with Various Conjugation Lengths (Lc)

Lc (rings)	V (meV)	λ (meV)
6	140.5	152.0
8	136.2	110.4
10	133.6	90.2

coupling (V) is insensitive to the conjugation length (Lc) if the positions of the conjugating domains are close to each other, yet a larger Lc generally favors the overlap of conjugating domains. In contrast, the reorganization energy (λ) correspond-ing to the electron−phonon coupling strength decreases sharply with increasing Lc, which results in a lower effective hopping barrier. These influences can be mapped onto the carrier mobility (μ) with μ increasing with decreasing λ and increasing V (Figure 3d). As defects have not been accounted for in this treatment, and the degree of irregularity in a realistic system is higher than that in our model, our calculated mobility is in reasonable agreement with experimental values (0.1−0.5 cm^2 V^{-1} s^{-1}).[10,29] Moreover, in response to various population
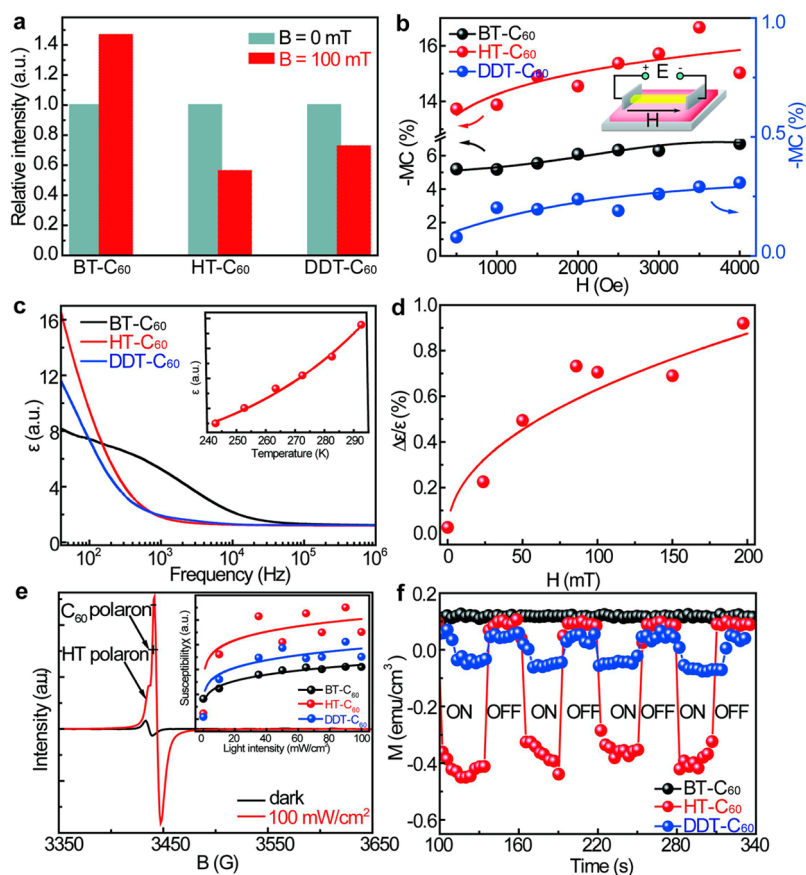
Figure 4. External stimuli control of optical, electrical, and ferroic properties. (a) Photoluminescence change for BT-C_{60}, HT-C_{60}, and DDT-C_{60} complexes without magnetic field and with magnetic field of 100 mT, respectively. (b) MC for BT-C_{60}, HT-C_{60}, and DDT-C_{60} complexes under different magnetic field. The applied electric field is 233 kV/cm. The inset is the measurement scheme of MC. (c) Frequency-dependent dielectric constant of HT-C_{60} crystal. The inset is the temperature-dependent dielectric constant change for HT-C_{60} crystal. (d) Magnetic field-dependent dielectric constant change for HT-C_{60} crystal at a frequency of 100 Hz. (e) Electron spin resonance spectra of HT-C_{60} under dark and light illumination at 100 mW/cm². The inset is the light intensity dependent susceptibility change for BT-C_{60}, HT-C_{60}, and DDT-C_{60} complexes. (f) Magnetoelectric coupling coefficient change for BT-C_{60}, HT-C_{60}, and DDT-C_{60} complexes under a electric field of 700 V/cm. The light intensity is 70 mW/cm². The magnetic field is 60 Oe.

distributions of phonon modes, the mobility first increases then decreases with increasing temperature, which is consistent with the negative temperature dependence reported for P3HT near room temperature.[29] The calculated mobility for C_{60} is also consistent with experimental values of 0.3–6 cm² V⁻¹ s⁻¹,[30,31] implying that it is possible to achieve charge balance between donor and acceptor by tuning the donor side-chains. These calculations are consistent with our experimental results that HT provides the highest robustness against shift and thus may lead to large electron coupling, which is evidenced by the largest conductivity for HT-C_{60} in comparison to the other two (Figure 3e and Figure S9). The side-chain dependent steric hindering effect on the effect of conductivity is also confirmed by the conducting AFM (c-AFM, Figure 3f), where the segregation between the DDT-rich donor phase and C_{60}-rich acceptor phase is larger than that of the other two (Figure 3f). To further confirm the polymeric crystallization and interfacial electron coupling effect, the side-chain dependent thermo-electric Seebeck coefficient is shown in Figure 3g. At room temperature, Seebeck coefficients of HT-C_{60} and DDT-C_{60} are 190 ± 10 and 110 ± 40 μV/K, respectively, while no detectable thermovoltage is measured from the BT-C_{60}. The Seebeck coefficients observed in HT-C_{60} crystals are among the highest reported for polymeric thermoelectric materials, which typically

ranged between tens to hundreds of microvolt per kelvin (Table S2).[32−38] It is known that bipolarons are the major charge carriers in doped polythiophenes.[39,40] As proposed by Bubnova et al., the Fermi levels, E_F, of amorphous bipolaron conducting polymers lies between the valence band and the bipolaron band, and the density of states (DOS) near E_F varies very little with respect to energy.[41] As the ordering increases, the bipolaron band starts to merge into the valence band and becomes empty, resulting in an increase in the DOS slope near E_F. Because the Seebeck coefficient is related to the slope of the DOS at E_F,[42] one would expect that increase in the crystallinity of bipolaron conducting polymers can lead to an enhanced Seebeck coefficient.

The relatively small dielectric constant in organic materials is beneficial for the formation of a large Coulomb capture radius with the generation of the CT state.[43] An external magnetic field can cause spin-mixing with the change of the ratio between singlet and triplet CT state, leading to the change of corresponding CT dependent properties.[44] As shown in Figure 4a and Figure S6, the emission intensity of the BT-C_{60} complex increases under an external magnetic field of 100 mT due to the induced triplet to singlet conversion, whereas it decreases for both HT-C_{60} and DDT-C_{60} crystals, suggesting the transfer of singlet to triplet CT state. We evaluate the magneto-

conductance (MC) to gain further understanding of the CT characters in the complex with different side chain length. Figure 4b and Figures S25−S34 demonstrate a negative MC under different external stimuli (the inset illustrates the measurement scheme of MC). The scattering reaction between triplet CT states and polarons decreases the mobility of polarons, resulting in the decrease of the current density under magnetic field within the HT-C_{60} and DDT-C_{60} crystals, deemed as the negative MC effect. The magnetic field induces a decrease of the triplet CT by transferring them to the singlet CT, leading to the negative MC effect with a decrease of the charge carrier density. As discussed in Figure 1, a short alkyl side chain benefits the formation of CT states and thus the HT-C_{60} crystal exhibits a larger MC than that of the DDT-C_{60} crystal. However, a relatively small MC effect is shown in the BT-C_{60} complex, which results from its lower crystallinity. In the CT complex, the collective electron transfer from donor to acceptor leads to the formation of dipoles, which can be tuned by external stimuli. The ordered noncentrosymmetric crystalline structure with the generation of long-range orientation of dipoles, and the large density of CT states are beneficial for organic CT ferroelectrics.[45,46] It is consistent with the results in the inset of Figure 2j that the loading of electric field increase the alignment of the dipoles toward the crystal growth direction. The HT-C_{60} crystal exhibits the optimum photoexcitation dependent polarization due to its ordered structure and relatively weak shielding effect from donating electrons to acceptors (Figure S34a). In addition, its dielectric constant decreases with increasing frequency due to the dielectric relaxation (Figure 4c). The HT-C_{60} crystal shows a large dielectric constant at low frequency, while the BT-C_{60} complex shows a small dielectric relaxation due to the short alkyl side chain induced relatively large CT density. The inset of Figure 4c shows that the dielectric constant increases with temperature, which is due to the thermally excited triplet excitons. As discussed in Figure 4a, an external magnetic field can induce the transfer of singlet to triplet CT states, in which the triplet excitons increase the dipoles as the magneto-dielectric coupling effect (Figure 4d). The charge transfer between the donor and acceptor phase, together with the spin formation, play an important role in the magnetism of the CT complexes. In particular, a large variety of electronic phases exist in π-electron systems, including charge density wave, spin density wave, electron−phonon coupling, spin−lattice coupling which could enable the coupling between charge and spin orders.[47] In order to examine the CT controlled spin properties, electron spin resonance (ESR) has been utilized to study the CT states under dark and photoexcitation conditions (Figure 4e and Figure S36). In comparison to the dark condition, two strong ESR signals ascribing to HT polaron[+] and C_{60} polaron[−] appear, revealing the strong CT and effective photoexcitation characteristic in the HT-C_{60} crystals. This phenomenon was also observed in two other complexes (Figure S36) and summarized by the light intensity dependent susceptibility change as shown in Figure 4e. As shown in Figure S42, the application of electric field increases the ME coupling coefficient of the CT complexes in which the HT-C_{60} crystal shows the optimum ME coupling coefficient. The optimum ME coefficient of 1.0×10^{-3} Oe·cm/V is observed in HT-C_{60} crystals under a bias magnetic field of 60 Oe at a light intensity of 70 mW/cm^2 (Figure 4f and Figure S41). In the long-range ordered $\pi-\pi$ stacking network, the spin orders and CT dipoles are directed along a specific direction, enabling the spin-charge composite ferroic orders at ambient

conditions.[48−50] The electric field induces an increase of CT states with the enhancement of the coupling between the spin and charge ferroic orders, leading to more spin along the magnetization direction as well as the increase of the ME coupling effect. The photoexcitation induced CT and ordering can further enhance the ME coupling in crystals. By contrast, the disordered structure of BT-C_{60} and weak CT interaction in DDT-C_{60} due to the hindering effect by the long alkyl side chain, the coupling of spin, and charge orders are relatively weaker than that in HT-C_{60}, resulting in a lower ME coupling.

In conclusion, we design and exploit chemically driven side-chain engineering for a new class of multifunctional organic CT superstructures, produced by antisolvent crystallization and drying mediated self-assembly. The unique crystallization characteristics and high degree of charge transfer endow the crystals with anisotropic optical properties, high Seebeck coefficient and external stimuli dependent ferroic properties. The mechanistic studies from the theoretical modeling confirm that high degree of crystallinity in the polymer phase and appropriate energy profile between neighboring molecules enhance electron coupling and conjugation length, and thus access high carrier mobility. Furthermore, a short donor−acceptor interfacial distance provides sufficient electronic coupling between the donor and acceptor orbitals, which is necessary for both charge separation and direct excitation of CT states. The proposed strategies in this study open up a new opportunity to chemically design organic CT materials for the development of all-organic interfacial electronics.[9,51]

Methods. The details for the synthesis of the solution and the growth of the crystals can be found in part 1 of the Supporting Information. DFT and MD calculations on electric and structural properties can be found in part 5 of the Supporting Information.

Conducting Atomic Force Microscopy. Bruker dimension icon atomic force microscopy equipped with Cr/Pt-coated Si probe (radius <25 nm, resonant frequency, 13 kHz) was used. A voltage of 5−10 V was applied.

Fluorescence Measurement. (1) For the angle-dependent fluorescence measurement, the samples containing the crystals were mounted on an Olympus IX73 inverted microscope. Fluorescence was excited with 4.3 μW of a 532 nm laser and collected with a Princeton Instruments ACTON SpectraPro 2500i/Spec-10 spectrometer using a 20× objective. The excitation polarization was aligned to the long axis of each crystal investigated, while a linear polarizer in the detection path was varied (0° parallel to the excitation polarization and 90° perpendicular). (2) For electrical measurements, the crystals were grown on ITO glass substrate. Two wire leads (tinned-copper) were attached to the surface of the ITO using conductive Ag epoxy. Next, the leads were connected to a Power Designs Inc. Model TP325 triple output DC power supply. For each voltage step, the system was allowed to equilibrate before the spectrum was collected.

Thermovoltage Measurement. Seebeck coefficient (thermopower) was measured using an in-house apparatus. Thin film samples were deposited on glass slides, which were placed on top of two Peltier stages. The temperature was detected by thermocouples and the thermovoltage across the samples was measured using a multimeter. One of the Peltier stages was kept at 273 K (25 °C) while the temperature of the other was varied between 267 and 280 K.

Polarization Measurement. Polarization hysteresis loops is obtained by Radiant Precision Premier LC-II at room temperature in air. The measurement frequency is 1000 Hz.

Dielectric Constant Measurement. Broadband Dielectric/Impedance spectrometer Agilent 4249A was used to get the capacitance in $40-10^6$ Hz between 243 and 293 K. The bias is 600 mV.

ESR Measurements. Bruker EMX (type:ER073) plus ESR spectrometer is used to get ESR signal. Spin susceptibility is calculated from ESR signals. The crystal powder samples are used for the ESR measurements.

Magnetic Hysteresis (M-H) Loop Measurement. Micro-Sense EV7 vibrating sample magnetometer (VSM) is carried out to obtain M-H loops and magnetoelectric coupling at room temperature.

MD Simulation. Classical MD simulations were performed in the constant NPT ensemble for 1 ns with a 0.5 fs time step using the LAMMPS package.[52]

DFT Simulation. Standard DFT method as implemented in the VASP[53] and Quantum Espresso[54] packages were used to obtain the electronic structures for polythiophene crystals and polymer-C60 interfaces. The absorption spectra were computed by RPA approach using the BerkeleyGW package.[55]

Charge Transfer Rate. The carrier hopping rates were calculated by full quantum treatment within the phonon-assisted nonadiabatic charge dynamics scenario.[26] The electron couplings were obtained by the anticrossing approach, whereas the reorganization spectra were computed by the phonon mode decomposition.[27]

ASSOCIATED CONTENT

Supporting Information

The Supporting Information is available free of charge on the ACS Publications website at DOI: 10.1021/acs.nanolett.6b00712.

Synthesis, structure, morphology, chemical analysis, optical, thermoelectric, ferroelectric, dielectric, and magnetoelectric properties of polythiophene-C_{60} charge transfer CT complex, DFT, and MD calculation on structure and electric properties of the crystals. (PDF)

AUTHOR INFORMATION

Corresponding Authors
*(J.G.) E-mail: jcg@mit.edu.
*(S.R.) E-mail: shenqiang.ren@temple.edu.

Author Contributions
B.X. and H.S.L carried out experiments and the modeling calculation and wrote the paper. H.Q.L., L.Z., and F.R. designed and took the thermovoltage measurement. A.W. and K.W. designed and took the fluorescence analysis. K.C. helped with the AFM and conducting AFM measurement. S.R. and J.G guided the project and edited the paper. All authors discussed the results and commented on the manuscript.

Author Contributions
B.X. and H.L. contributed equally to this paper.

Notes
The authors declare no competing financial interest.

ACKNOWLEDGMENTS

REFERENCES

(1) Bibes, M. *Nat. Mater.* **2012**, *11* (5), 354.
(2) Cuellar, F. A.; Liu, Y. H.; Salafranca, J.; Nemes, N.; Iborra, E.; Sanchez-Santolino, G.; Varela, M.; Garcia Hernandez, M.; Freeland, J. W.; Zhernenkov, M.; Fitzsimmons, M. R.; Okamoto, S.; Pennycook, S. J.; Bibes, M.; Barthelemy, A.; te Velthuis, S. G.; Sefrioui, Z.; Leon, C.; Santamaria, J. *Nat. Commun.* **2014**, *5*, 4215.
(3) Naber, R. C. G.; Tanase, C.; Blom, P. W. M.; Gelinck, G. H.; Marsman, A. W.; Touwslager, F. J.; Setayesh, S.; de Leeuw, D. M. *Nat. Mater.* **2005**, *4* (3), 243.
(4) Wen, Z.; Li, C.; Wu, D.; Li, A.; Ming, N. *Nat. Mater.* **2013**, *12* (7), 617.
(5) Miyasaka, H. *Acc. Chem. Res.* **2013**, *46* (2), 248.
(6) Yamamoto, T. *NPG Asia Mater.* **2010**, *2* (2), 54.
(7) Coleman, L. B.; Cohen, M. J.; Sandman, D. J.; Yamagishi, F. G.; Garito, A. F.; Heeger, A. J. *Solid State Commun.* **1973**, *12* (11), 1125.
(8) Lappas, A.; Prassides, K.; Vavekis, K.; Arcon, D.; Blinc, R.; Cevc, P.; Amato, A.; Feyerherm, R.; Gygax, F. N.; Schenck, A. *Science* **1995**, *267*, 1799−1782.
(9) Xu, B.; Li, H.; Hall, A.; Gao, W.; Gong, M.; Yuan, G.; Grossman, J.; Ren, S. *Sci. Adv.* **2015**, *1* (11), e1501264.
(10) Sauve, G.; Javier, A. E.; Zhang, R.; Liu, J.; Sydlik, S. A.; Kowalewski, T.; McCullough, R. D. *J. Mater. Chem.* **2010**, *20* (16), 3195.
(11) Huang, W. Y.; Lee, C. C.; Wang, S. G.; Han, Y. K.; Chang, M. Y. *J. Electrochem. Soc.* **2010**, *157* (9), B1336.
(12) Pankaj, S.; Hempel, E.; Beiner, M. *Macromolecules* **2009**, *42* (3), 716.
(13) Wu, P.-T.; Ren, G.; Jenekhe, S. A. *Macromolecules* **2010**, *43* (7), 3306.
(14) Kline, R. J.; DeLongchamp, D. M.; Fischer, D. A.; Lin, E. K.; Richter, L. J.; Chabinyc, M. L.; Toney, M. F.; Heeney, M.; McCulloch, I. *Macromolecules* **2007**, *40* (22), 7960.
(15) Reddy, S. Y.; Kuppa, V. K. *Synth. Met.* **2012**, *162* (23), 2117.
(16) Huang, D. M.; Faller, R.; Do, K.; Moule, A. J. *J. Chem. Theory Comput.* **2010**, *6* (2), 526.
(17) McMahon, D. P.; Cheung, D. L.; Troisi, A. *J. Phys. Chem. Lett.* **2011**, *2* (21), 2737.
(18) Northrup, J. E. *Phys. Rev. B: Condens. Matter Mater. Phys.* **2007**, *76* (24), 245202.
(19) Cheung, D. L.; McMahon, D. P.; Troisi, A. *J. Phys. Chem. B* **2009**, *113* (28), 9393.
(20) Nguyen, L. H.; Hoppe, H.; Erb, T.; Guenes, S.; Gobsch, G.; Sariciftci, N. S. *Adv. Funct. Mater.* **2007**, *17* (7), 1071.
(21) Campoy-Quiles, M.; Ferenczi, T.; Agostinelli, T.; Etchegoin, P. G.; Kim, Y.; Anthopoulos, T. D.; Stavrinou, P. N.; Bradley, D. D. C.; Nelson, J. *Nat. Mater.* **2008**, *7* (2), 158.
(22) Li, G.; Shrotriya, V.; Huang, J.; Yao, Y.; Moriarty, T.; Emery, K.; Yang, Y. *Nat. Mater.* **2005**, *4* (11), 864.
(23) Li, L.-H.; Kontsevoi, O. Y.; Freeman, A. J. *J. Phys. Chem. C* **2014**, *118* (19), 10263.
(24) Al-Ibrahim, M.; Roth, H. K.; Schroedner, M.; Konkin, A.; Zhokhavets, U.; Gobsch, G.; Scharff, P.; Sensfuss, S. *Org. Electron.* **2005**, *6* (2), 65.
(25) Lan, Y.-K.; Huang, C.-I. *J. Phys. Chem. B* **2008**, *112* (47), 14857.
(26) Jortner, J. *J. Chem. Phys.* **1976**, *64* (12), 4860.
(27) Li, H.; Wu, Z.; Lusk, M. T. *J. Phys. Chem. C* **2014**, *118* (1), 46.
(28) Kawai, T.; Nakazono, M.; Sugimoto, R.; Yoshino, K. *J. Phys. Soc. Jpn.* **1992**, *61* (9), 3400.
(29) Joshi, S.; Pingel, P.; Grigorian, S.; Panzner, T.; Pietsch, U.; Neher, D.; Forster, M.; Scherf, U. *Macromolecules* **2009**, *42* (13), 4651.

(30) Singh, T. B.; Sariciftci, N. S.; Yang, H.; Yang, L.; Plochberger, B.; Sitter, H. *Appl. Phys. Lett.* **2007**, *90* (21), 213512.

(31) Kobayashi, S.; Takenobu, T.; Mori, S.; Fujiwara, A.; Iwasa, Y. *Appl. Phys. Lett.* **2003**, *82* (25), 4581.

(32) Yan, H.; Ohta, T.; Toshima, N. *Macromol. Mater. Eng.* **2001**, *286* (3), 139.

(33) Park, Y. W. *Synth. Met.* **1991**, *45* (2), 173.

(34) Zhang, Q.; Sun, Y.; Xu, W.; Zhu, D. *Energy Environ. Sci.* **2012**, *5* (11), 9639.

(35) Hu, D.; Liu, Q.; Tisdale, J.; Lei, T.; Pei, J.; Wang, H.; Urbas, A.; Hu, B. *ACS Nano* **2015**, *9* (5), 5208.

(36) Bubnova, O.; Khan, Z. U.; Malti, A.; Braun, S.; Fahlman, M.; Berggren, M.; Crispin, X. *Nat. Mater.* **2011**, *10* (6), 429.

(37) Kim, G. H.; Shao, L.; Zhang, K.; Pipe, K. P. *Nat. Mater.* **2013**, *12* (8), 719.

(38) Liu, Q.; Hu, D.; Wang, H.; Stanford, M.; Wang, H.; Hu, B. *Phys. Chem. Chem. Phys.* **2014**, *16* (40), 22201.

(39) Bertho, D.; Jouanin, C. *Phys. Rev. B: Condens. Matter Mater. Phys.* **1987**, *35* (2), 626.

(40) Sai, N.; Li, Z. Q.; Martin, M. C.; Basov, D. N.; Di Ventra, M. *Phys. Rev. B: Condens. Matter Mater. Phys.* **2007**, *75* (4), 045307.

(41) Bubnova, O.; Khan, Z. U.; Wang, H.; Braun, S.; Evans, D. R.; Fabretto, M.; Hojati-Talemi, P.; Dagnelund, D.; Arlin, J.-B.; Geerts, Y. H.; Desbief, S.; Breiby, D. W.; Andreasen, J. W.; Lazzaroni, R.; Chen, W. M.; Zozoulenko, I.; Fahlman, M.; Murphy, P. J.; Berggren, M.; Crispin, X. *Nat. Mater.* **2013**, *13* (2), 190.

(42) Snyder, G. J.; Toberer, E. S. *Nat. Mater.* **2008**, *7* (2), 105.

(43) Clarke, T. M.; Durrant, J. R. *Chem. Rev.* **2010**, *110* (11), 6736.

(44) Hu, B.; Yan, L.; Shao, M. *Adv. Mater.* **2009**, *21* (14−15), 1500.

(45) Tayi, A. S.; Shveyd, A. K.; Sue, A. C. H.; Szarko, J. M.; Rolczynski, B. S.; Cao, D.; Kennedy, T. J.; Sarjeant, A. A.; Stern, C. L.; Paxton, W. F.; Wu, W.; Dey, S. K.; Fahrenbach, A. C.; Guest, J. R.; Mohseni, H.; Chen, L. X.; Wang, K. L.; Stoddart, J. F.; Stupp, S. I. *Nature* **2012**, *488* (7412), 485.

(46) Tayi, A. S.; Kaeser, A.; Matsumoto, M.; Aida, T.; Stupp, S. I. *Nat. Chem.* **2015**, *7* (4), 281.

(47) Enoki, T.; Miyazaki, A. *Chem. Rev.* **2004**, *104* (11), 5449.

(48) Ren, S.; Wuttig, M. *Adv. Mater.* **2012**, *24* (6), 724.

(49) Lunkenheimer, P.; Müller, J.; Krohns, S.; Schrettle, F.; Loidl, A.; Hartmann, B.; Rommel, R.; de Souza, M.; Hotta, C.; Schlueter, J. A.; Lang, M. *Nat. Mater.* **2012**, *11* (9), 755.

(50) van den Brink, J.; Khomskii, D. I. *J. Phys.: Condens. Matter* **2008**, *20* (43), 434217.

(51) Mei, J.; Bao, Z. *Chem. Mater.* **2014**, *26* (1), 604.

(52) Plimpton, S. *J. Comput. Phys.* **1995**, *117* (1), 1.

(53) Kresse, G.; Furthmuller, J. *Phys. Rev. B: Condens. Matter Mater. Phys.* **1996**, *54* (16), 11169.

(54) Giannozzi, P.; Baroni, S.; Bonini, N.; Calandra, M.; Car, R.; Cavazzoni, C.; Ceresoli, D.; Chiarotti, G. L.; Cococcioni, M.; Dabo, I.; Dal Corso, A.; de Gironcoli, S.; Fabris, S.; Fratesi, G.; Gebauer, R.; Gerstmann, U.; Gougoussis, C.; Kokalj, A.; Lazzeri, M.; Martin-Samos, L.; Marzari, N.; Mauri, F.; Mazzarello, R.; Paolini, S.; Pasquarello, A.; Paulatto, L.; Sbraccia, C.; Scandolo, S.; Sclauzero, G.; Seitsonen, A. P.; Smogunov, A.; Umari, P.; Wentzcovitch, R. M. *J. Phys.: Condens. Matter* **2009**, *21* (39), 395502.

(55) Deslippe, J.; Samsonidze, G.; Strubbe, D. A.; Jain, M.; Cohen, M. L.; Louie, S. G. *Comput. Phys. Commun.* **2012**, *183* (6), 1269.